

Topology optimization of a superabsorbing thin-film semiconductor metasurface

Johannes Gedeon, Izzatjon Allayarov, Emadeldeen Hassan, and Antonio Calà Lesina

Abstract—We demonstrate a computational inverse design method for optimizing broadband-absorbing metasurfaces made of arbitrary dispersive media. Our figure of merit is the time-averaged instantaneous power dissipation in a single unit cell within a periodic array. Its time-domain formulation allows capturing the response of arbitrary dispersive media over any desired spectral range. Employing the time-domain adjoint method within a topology optimization framework enables the design of complex metasurface structures exhibiting unprecedented broadband absorption. We applied the method to a thin-film Silicon-insulator configuration and explored the impact of structural and (time-domain inherent) excitation parameters on performance over the visible–ultraviolet. Since our incorporated material model can represent any linear material, the method can also be applied to other all-dielectric, plasmonic, or hybrid configurations.

Index Terms—Absorption, adjoint method, complex-conjugate pole–residue pairs model, FDTD method, inverse design, metasurface, optical dispersion, quasi-guided modes, silicon, surface lattice resonances, time domain, topology optimization

I. INTRODUCTION

Thin-film absorbing metasurfaces are of great interest for both fundamental research and engineering, as they can efficiently capture light across a broad spectrum while reducing material resource use. Among the various potential applications, they attract the most attention in the field of solar energy harvesting. [1], [2], [3]. To date, numerous studies are being conducted to improve light trapping in (nano-) photonic devices to achieve broadband absorption, and different architectures and material combinations have been proposed. These include metacoatings exhibiting graded refractive index profiles [4], hybrid metal-dielectric–metal stacks for surface plasmon coupling [5], and supercells that achieve improved multi- and broadband control [6], to name just a few.

All-dielectric absorbers, however, rely on complexly shaped resonators that exhibit multiple resonances and their efficient coupling [7], [8]. Pala et al. [7] demonstrated that using waveguide geometries as subwavelength elements can enhance light trapping over a broad bandwidth. As experimentally proved, their thin-film designs exhibit a remarkable increase in short-circuit current, making them attractive for photovoltaic applications. This boost in absorption comes from a combination of localized Mie resonances and delocalized resonant waveguide modes. While Mie resonances emerge in single

This work was supported by the Deutsche Forschungsgemeinschaft (DFG, German Research Foundation) under Germany’s Excellence Strategy within the Cluster of Excellence PhoenixD (EXC 2122, Project ID 390833453), and within the Research Grant CA 2763/2-1 (Project ID 527470210). The computing time was granted by the Resource Allocation Board and provided on the supercomputer Lise and Emmy/Grete at NHR@ZIB and NHR@Göttingen as part of the NHR infrastructure. The calculations for this research were conducted with computing resources under the project nip00059.

Johannes Gedeon, Izzatjon Allayarov and Antonio Calà Lesina are with the Hannover Centre for Optical Technologies, the Institute for Transport and Automation Technology (Faculty of Mechanical Engineering), and the Cluster of Excellence PhoenixD, Leibniz University Hannover, 30167 Hannover, Germany (e-mail: johannes.gedeon@hot.uni-hannover.de; antonio.calalesina@hot.uni-hannover.de).

Emadeldeen Hassan is with the Department of Applied Physics and Electronics, Umeå University, SE-901 87 Umeå, Sweden (e-mail: emadeldeen.hassan@umu.se).

meta-atoms [9], delocalized modes originate from collective effects due to the array configuration of a metasurface. These include surface lattice resonances (SLRs) and the above-mentioned (quasi) guided modes (QGMs) [10]. SLRs arise from the coupling of resonances in meta-atoms (which need not be physically interconnected) by the in-plane diffraction orders of the lattice. They appear when the diffraction order becomes an evanescent wave, known as the Rayleigh anomaly (RA). QGMs are commonly not distinguished from SLRs in the literature; however, they require a waveguide structure with a higher refractive index than the surrounding medium. In Ref. [7], such QGMs were employed in periodically arranged ridge and trapezoidal waveguide structures to boost broadband absorption. These structures were found using traditional design methods that rely on intuitive physical insights and parameter sweeps of geometrical features. However, this approach can be time-consuming and computationally expensive.

In recent years, inverse design methods have emerged as a powerful alternative, where the structural design is dictated by the desired optical response itself [11]. However, broadband optimization still poses significant challenges for methods developed in the frequency domain [12]. In a recent work [9], we introduced a novel gradient-based inverse design method employing topology optimization (TopOpt) to enhance broadband absorption in dispersive nanoparticles. Our approach leverages the adjoint method in the *time domain* to efficiently compute gradients over any desired spectral range, enabling the design to evolve into a structure that inherently accounts for frequency-dependent material responses over a broad spectrum. This method promises to be efficient for designing thin-film all-dielectric absorbers as well.

In this article, we demonstrate our TopOpt method for the design of a superabsorbing Silicon metasurface in the visible–ultraviolet range. Our method allows us to optimize a metasurface beyond the limitations of conventional geometries, resulting in unprecedented topologies and phenomena that can also inspire other (conventional) design approaches. To explore the theoretical limits of broadband absorption, we enable free-form optimization in 3D; and in this context, we provide physical insight into both improvements and limitations in achieving uniform absorption.

II. COMPLEX-CONJUGATE POLE-RESIDUE PAIRS AND INSTANTANEOUS POWER DISSIPATION IN DISPERSIVE MEDIA

To enable the inverse design of absorbing metasurfaces, we build on our recent contributions from Refs. [13], [9]. Herein, we introduced a time-domain adjoint scheme for the design of nanostructures of arbitrary, dispersive media, which are described by the complex-conjugate pole residue (CCPR) pairs model [14],

$$\varepsilon(\omega) = \varepsilon_\infty + \frac{\sigma}{j\omega\varepsilon_0} + \sum_{p=1}^P \left(\frac{c_p}{j\omega - a_p} + \frac{c_p^*}{j\omega - a_p^*} \right). \quad (1)$$

The coefficients a_p and c_p can be complex (with * denoting complex conjugation). Selecting the number of poles P appropriately allows the model to accurately fit the complex permittivity of a linear material over an arbitrary frequency range. The coefficients for fitting

Silicon's permittivity in the range 300–700 nm are given in Table I, with only two poles used. Fig. 1 demonstrates the excellent agreement between the modeled complex permittivity and the experimental measurements.

Parameter	Fitting value
ε_∞	1
σ	0
a_1	$-8.00 \times 10^{14} + 6.39 \times 10^{15}j$
c_1	$7.31 \times 10^{14} - 2.89 \times 10^{16}j$
a_2	$-2.32 \times 10^{14} + 5.12 \times 10^{15}j$
c_2	$4.68 \times 10^{15} - 4.55 \times 10^{15}j$

TABLE I: CCPR parameters for modeling Silicon's permittivity ε in the wavelength range 300-700 nm, using two poles.

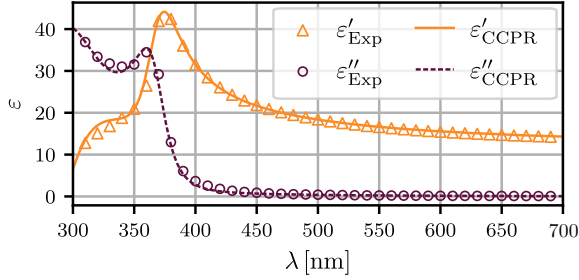


Fig. 1: Real and imaginary part of the permittivity $\varepsilon = \varepsilon' - j\varepsilon''$ of Silicon, reproduced by the CCPR model (1) using the coefficients listed in Table I. The experimental data was taken from Ref. [15].

We integrated this model into the time-domain Maxwell's equations by employing the auxiliary differential equations (ADEs) method [16]. It allows us to accurately capture the material response over the spectral range covered in the time signal of excitation. These equations formed the basis for our derived adjoint scheme to enable gradient-based TopOpt [17] that is used to find an optimal material distribution that maximizes a specified objective. Due to the universality of the CCPR model, the framework provides maximum flexibility when handling dispersive media for broadband optimization. Furthermore, we outlined how the algorithm can be incorporated into the Finite-Difference Time-Domain (FDTD) method - a widely used computational tool for modeling electrodynamic phenomena [18].

Dispersion is inherently linked to material losses [19], which cause power dissipation in dispersive nanostructures. In our recent work [9], we found that the *instantaneous power dissipation density* based on the CCPR-ADE formulation reads

$$q_e(t) = \sigma \mathbf{E}^2 + 2 \sum_{p=1}^P \Re \left\{ \frac{(\partial_t \mathbf{Q}_p)^2}{\varepsilon_0 c_p} \right\}, \quad (2)$$

where \mathbf{E} is the electric field, and \mathbf{Q}_p denotes the auxiliary field associated with a CCPR pole. The time-averaged loss in the nanostructure can then be calculated using

$$F := \frac{1}{T} \int_{\Omega_o \times I} q_e(t, \mathbf{r}) dt d^3 r, \quad (3)$$

where $I = [0, T]$ is a time interval, and Ω_o represents the observation region. Given the spectral content conveyed by the excitation time signal, it accounts for the absorptive response across the entire frequency range. This expression serves as the objective function for the metasurface optimization presented in this article.

III. SETUP

For the demonstration of our method, we choose a thin-film Silicon-on-insulator configuration as in Fig. 2 (a). The design domain

coincides with a single unit cell of an infinitely extended periodic metasurface, surrounded by air and SiO₂. Here, the Silicon metasurface is shown as a ridge structure only for illustration purposes. This conventional design studied in Ref. [7] is used as a benchmark to evaluate the performance of our actual TopOpt design. We consider a constant refractive index for air ($n = 1$) and SiO₂ ($n=1.45$), and the permittivity of Silicon ε_{Si} modeled by the CCPR (1) with its coefficients given in Table I.

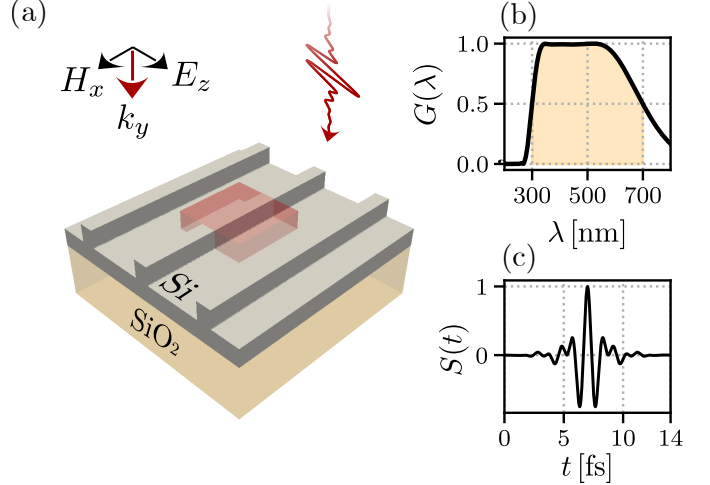


Fig. 2: Sketch of the optimization setup. (1) The red cuboid marks our design region and represents a single unit cell of the periodic Silicon (Si) metasurface, enclosed by SiO₂ and air. The system is excited by a light pulse, covering the (b) wavelengths 300-700 nm (marked in yellow) through the (c) time signal.

We aim to maximize the absorption of power delivered by a z -polarized plane wave at normal incidence over the wavelength range 300–700 nm. This is achieved by maximizing the time-averaged instantaneous power dissipation, Eq. (3), integrated over the unit cell, while imposing periodic boundary conditions (PBC). The time T in Eq. (3) is chosen such that the time-domain fields are sufficiently decayed and no longer contribute to a substantial increase in the objective. During the optimization, the system is excited by a short pulse governed by a tailored time signal. This time signal covers the entire spectral range of interest, as shown in Fig. 2 (b) & (c).

We employ a density-based TopOpt [17] and our adjoint formulation [13] to find an optimal material distribution that maximizes the absorption over broad range. The optimization algorithm iteratively updates the design in the form of a density distribution $\rho(\mathbf{r}) \in [0, 1]$ within the unit cell. The density represents a linear interpolation of both permittivities of air and Silicon, $\varepsilon_{\text{Mix}} = \rho \varepsilon_{\text{Si}} + (1 - \rho) \varepsilon_{\text{Air}}$. We note that ε_{Mix} is frequency-dependent, but recall that due to our time-domain adjoint formulation using CCPR-ADEs, the algorithm inherently accounts for dispersion and material loss across the entire spectral range of interest. As the optimization progresses, the density distribution gradually converges towards a binary structure, where values of $\rho = 1$ correspond to the design material and $\rho = 0$ to the background material. At the end of the optimization, the density is binarized based on a threshold to obtain the final structure. We then evaluate the broadband performance of the designed metasurface by analyzing its absorption spectrum (using Lumerical's FDTD solver [20]).

All following optimizations are conducted using an in-house parallelized FDTD solver [21] with TopOpt implementation. The FDTD and TopOpt configuration settings are adapted from the Silicon particle optimization described in Ref. [13]. All presented designs

are openly available (as STL format) [22] and can be integrated into an electromagnetic solver to validate our results. In the following, we will explicitly specify optimization parameters of only significant importance. Moreover, if we refer to "the design" (or structure) in our descriptions, it is always meant in the context of its periodic arrangement throughout this article.

IV. RESULTS AND DISCUSSION

A. A first demonstration

We first apply our method to the design of a Silicon metasurface of thickness $d = 200$ nm, having a quadratic unit cell with periodicity $a = 400$ nm. With the discretization we chose within the FDTD method, this results in 1.5×10^6 degrees of freedom of the design to evolve. The performance is compared with a conventional Ridges structure as reported in Ref. [7] as a reference. Our TopOpt configuration allows the evolution to metasurfaces exploiting SLRs or QGMs as collective effects to enhance absorption, which were briefly explained in the introduction. To maintain generality, we hereafter refer to SLRs and QGMs collectively as lattice resonances (LRs), given that both phenomena can emerge in principle and both are dictated by the RA.

As the initial density, we choose a cylinder ($\rho = 0.5$) embedded in a homogeneous environment ($\rho = 0.4$) that fills the entire unit cell. Fig. 3 shows the convergence of the optimization over 70 iterations, tracking the objective in Eq. (2) for the evolving structure normalized to that of the Ridges. The density steadily progressed toward a binary design. After applying the final thresholding, we obtained an enhancement factor of 2.45. We note that starting with a *homogeneous* density across the entire unit cell prevents the design from evolving into a complex 3D structure, as all fields become in-plane invariant due to our physical setup (Fig. 2). In that case, the converging density exhibits a layered profile similar to that of metacoatings [4].

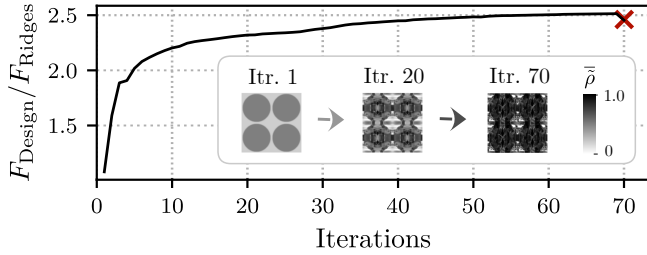


Fig. 3: Convergence plot of the optimization. F_{Design} is the time-averaged measured power dissipation of the evolving structure, normalized to that of a conventional Ridges (F_{Ridges}). The subfigure presents top views of the (filtered and projected [23]) density $\bar{\rho}$ arranged in a 2×2 array, capturing the metasurface's evolution. At the last iteration, a thresholding was applied to yield the binary design (marked by a red cross).

Interestingly, the periodic arrangement of the unit cell's optimized material distribution forms a waveguide pattern as of the Ridges metasurface. We compared their broadband performance by analyzing their absorption spectrum in Fig. 4(b). Our TopOpt design shows a remarkable broadband performance, reaching its absorption peak $A_{\text{Max}} = 0.97$ at $\lambda = 400$ nm. It outperforms the conventional Ridges structure over the entire wavelength range 300-700 nm, demonstrating the success and strength of the inverse design method. As it was already observed in Ref. [7], the Ridges exhibit two characteristic absorption peaks around $\lambda = 600$ nm, attributed to coupling with waveguide modes. Similar features also appear in our

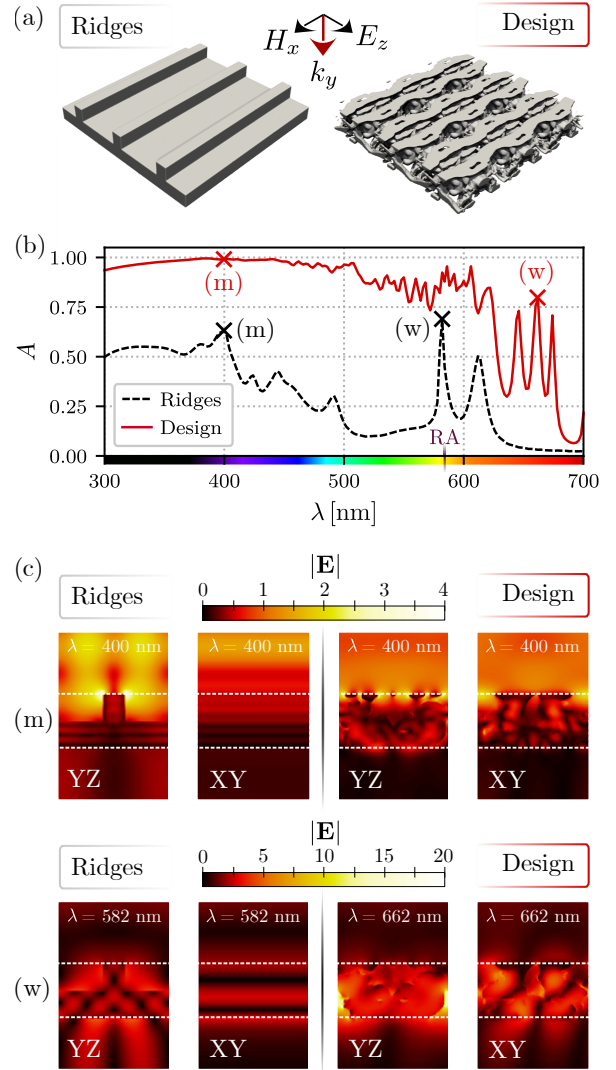


Fig. 4: Comparison of a conventional Ridges design with our TopOpt metasurface from Fig. 3. (a) Illustration of both metasurfaces by showing a section of 9 adjacent unit cells, and (b) their absorption spectrum over the wavelength range of interest. Here, 'RA' denotes SiO₂'s first-order Rayleigh anomaly at $\lambda^{\text{RA}} = 584$ nm. The crosses mark absorption maxima associated with Mie resonances '(m)' and waveguide modes '(w)'; and (c) displays cross-sections of the corresponding electric field's magnitude in a unit cell of both metasurfaces. The boundaries of the Silicon thin-film are marked as white dashed lines.

TopOpt design in the red region $\lambda > 630$ nm. We identified and labeled resonances associated with localized Mie resonances as '(m)' and those attributed to waveguide modes as '(w)'. The corresponding cross-sections of the time-harmonic electric field magnitude $|\mathbf{E}|$ in one unit cell are visualized in Fig. 4(c). Comparing the profile associated with the Mie resonances at $\lambda = 400$ nm in both structures (1st row), we observe enhanced light trapping in the complex, branched TopOpt design compared to the Ridges, characterized by numerous diffusely distributed hotspots. In contrast, the electric field distribution corresponding to their characteristic absorption peaks (2nd row) resembles a profile typically observed in waveguide geometries (see XY cross-section).

The absorption spectrum of the TopOpt metasurface reveals a

performance profile similar to that previously observed in the single-particle optimization reported in Ref. [9]: the design shows strong performance in the (ultra) violet regime but declines towards the (infra) red. The optimizer leverages Silicon’s intrinsic material’s losses toward the (ultra) violet. This is the region where interband transitions can occur, and are indicated by an increased imaginary part of the permittivity ϵ'' in Fig. 1. In a thin-film-on-insulator configuration (as ours), the semiconductor can even support plasmonic resonances in the ultraviolet [24] - a phenomenon typically associated with metals. Given the algorithm’s gradient-based nature and the specified spectral weighting (Fig. 2(b)), it efficiently directs the design to evolve toward a structure that attains a (local) maximum of the objective Eq. (3), exhibiting broadband absorption across the inherently prioritized wavelengths. This is the signature trait of the time-domain approach and what fundamentally distinguishes it from the commonly used (hybrid) frequency-domain methods [12].

Our optimization result suggests that the optimizer exploits LRs over broad range to boost absorption towards red, as indicated in Fig. 4 by the emergence of sharper features in the absorption spectrum around the substrate’s first-order RA at $\lambda^{\text{RA}} = a \cdot n_{\text{SiO}_2} = 584 \text{ nm}$ [25] (b), and by the evolved waveguide-like pattern (a). However, LRs’ mode density and strength highly depend on periodicity and thin-film thickness [26], and likely on the induced spectral weighting of the time signal under which the design evolves. Therefore, we examine the influence of structural and excitation parameters on broadband performance, offering deeper insights into potential improvements and the fundamental nature of a time-domain approach.

B. Effects of the Unit Cell Dimensions and Spectral Weighting on Performance

Motivated by observations from the previous section, we explore the impact of unit cell dimensions as optimization constraints on broadband performance. Additionally, we examine the impact of spectral weighting conveyed by the time signal during optimization.

Fig. 5 presents the optimization results for the different hyperparameter settings, including periodicity a and thickness d and excitation spectrum. The spectral weighting is shown in (a), the designs in top view in (b), and their absorption spectra in (c). The wavelength range 300-700 nm, over which we aim to boost absorption, is hereafter called *region of interest* (ROI). The optimized metasurface and its configuration from the previous section serve as a reference for comparison across all parametric sweeps. Rapid variations in the absorption curves make a direct comparison of broadband performance challenging. We introduced a quantitative measure in Appendix A to address this issue. In the following, we focus primarily on qualitative comparisons to observe performance trends as we vary the hyperparameters - with the quantitative measures summarized in Table II.

From the change in periodicity (Fig. 5, 1st row), we observe an improved performance beyond $\lambda > 620 \text{ nm}$ for the periodicities 400 nm and 600 nm compared to 200 nm. In this range, characteristic sharp absorption spikes emerged, which we attribute to LRs. Both substrate (n_{SiO_2}) and superstrate (air) have their own RA at $\lambda_{\text{SiO}_2}^{\text{RA}} = 1.45 \cdot a$ and $\lambda_{\text{air}}^{\text{RA}} = a$. As the RA wavelengths redshift with increasing periodicity, the emergence of the spikes for both periodicities with $a > 200 \text{ nm}$ but absence for $a = 200 \text{ nm}$ can be explained. The LRs can only arise and be leveraged by the optimizer if the λ^{RA} s shift to the red regime, which was achieved as we increased the lattice constant. Across the ROI, no broadband improvement can be stated for a periodicity of 600 nm relative to 400 nm. As we noted an increase in our time-domain objective, however, we attribute this

to the optimizer considering wavelengths across the entire excitation spectrum (see Fig. 5 (a), 1st row), including those beyond the ROI where the substrate’s Rayleigh anomaly occurs (at 870 nm).

An improvement in broadband performance is clearly evident when increasing the thickness of the thin-film design layer (Fig. 5, 2nd row). In fact, the design with $d = 300 \text{ nm}$ exhibits the best performance among all metasurfaces presented in this article. This tendency of improvement is expected. Initially, the optimizer is provided with more lossy material per unit cell to utilize. The out-of-plane extension of the unit cell increases the number of degrees of freedom for the evolving metasurface. Thus, it allows the formation of resonances at longer wavelengths and of higher-order localized and delocalized modes (with potential hybridization). We observed a denser clustering of absorption peaks in the red with increasing thickness, indicating a higher mode density of the LRs.

Lastly, we study the dependence of performance on the spectral weighting under which the designs have evolved (Fig. 5, 3rd row). Each spectrum in (a) belongs to a different spectral amplitude profile $G(\lambda)$, which was conveyed by the time signal of excitation during optimization. We labeled them by the letters ‘A’, ‘B’ and ‘C’. Spectrum ‘B’ is identical to that of Fig. 2 (b), and was used in all optimization of the sweeps over periodicity and thickness. Spectrum ‘C’ provides a uniform weighting across the ROI and gives extra emphasis to wavelengths near the ROI’s bounds relative to spectrum ‘B’. Comparing both absorption spectra exhibited by the designs, we do not observe an overall improvement by this adjustment. This is not surprising, given our previous explanation that the optimization algorithm inherently prioritizes those wavelengths associated with greater material loss, i.e., primarily across the (ultra) violet. More interesting, however, is the evaluation of the performance of the design evolved under spectrum ‘A’. Spectrum ‘A’ spans a wavelength range that only partially overlaps with the ROI. Its lower (half-maximum) bound is $\lambda_{1/2} = 600 \text{ nm}$. In that case, Silicon’s characteristic intrinsic losses cannot be leveraged during the optimization process. As we observe, the design shows a significantly reduced performance for wavelengths below 600 nm, matching the spectral weight’s lower bound $\lambda_{1/2}$. Above that wavelength, its absorption is considerably higher and even exhibits absorption spikes that approach unity. This example demonstrates the effect of spectral weighting as a constraint. Initially, the optimizer can only utilize the material’s intrinsic (dispersive) response over the conveyed wavelengths. It relies on the exploitation of physical effects in that weighted spectrum to boost absorption most efficiently. For spectrum ‘A’, and given the initial (periodic) physical configuration, these are primarily the lattice-induced effects.

From this study on hyperparameters, we conclude: broadband performance can be improved through proper spectral weighting and by expanding the design’s degrees of freedom. However, dissipation is fundamentally bounded by both the design’s dimension and the material’s intrinsic losses, limiting the extent to which absorption can be maximized [27], [28]. The achieved enhancement towards the red is accompanied by the emergence of narrow-band features and rapid spectral fluctuations associated with the LRs. This highlights the efficient exploitation of lattice effects by the time-domain adjoint method but also reveals the physical limitations of achieving uniform absorption.

V. CONCLUSION

We enabled the inverse design of a superabsorbing semiconductor metasurface in the visible-to-ultraviolet spectral range. Starting from a thin-film silicon-on-glass configuration, we achieved this by (1) modeling silicon via CCPR and (2) employing our (FDTD) time-domain CCPR-ADE adjoint method to maximize the time-averaged

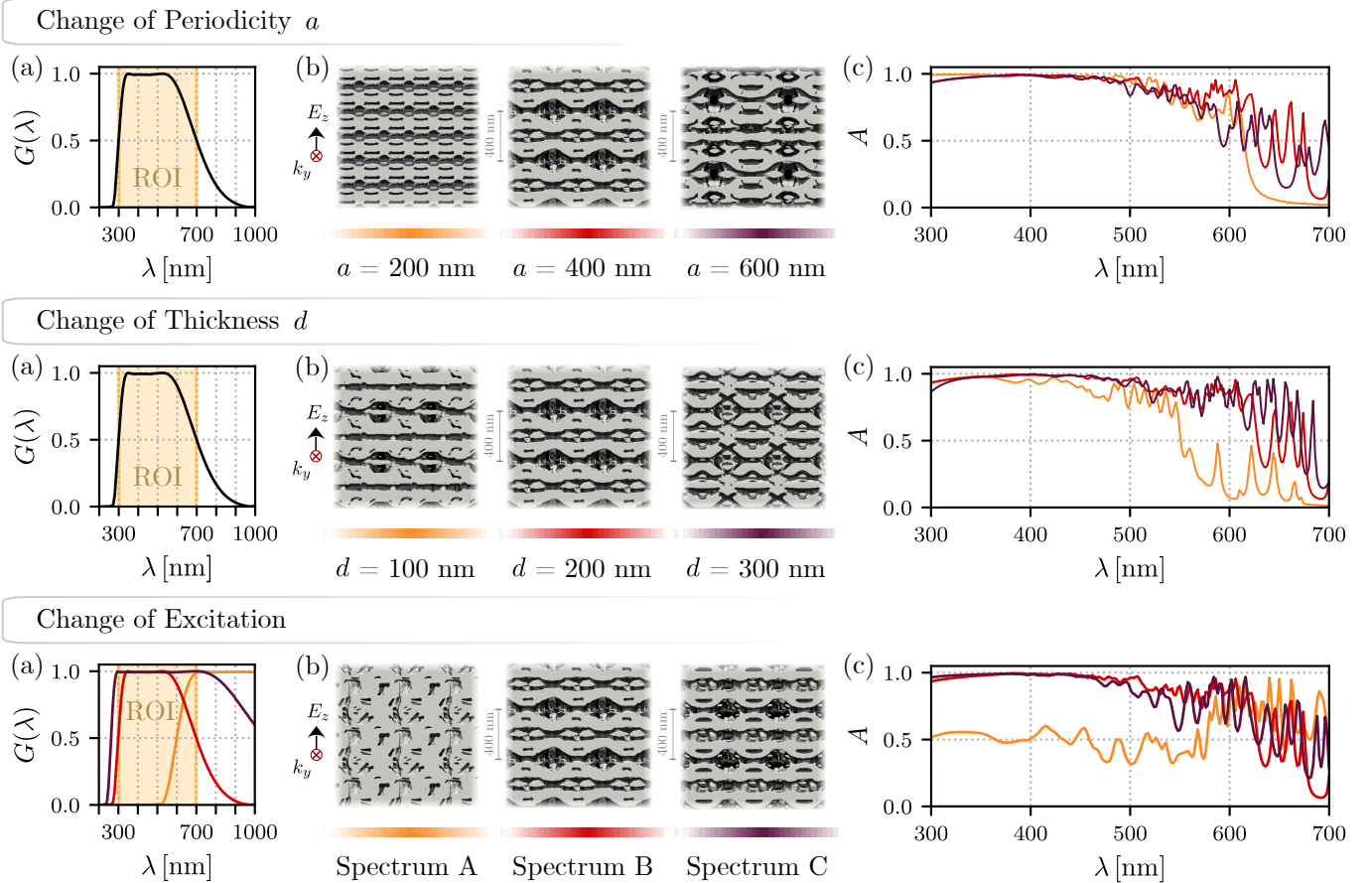


Fig. 5: Optimization results for different configurations of periodicity a (1st row), thickness d (2nd row) and spectral weighting (3rd row) considered in the metasurface design. Each row represents a parametric sweep where one parameter varies while the other two remain fixed. The structure consistently shown across all sweeps (marked in red) corresponds to the original configuration from Fig. 4 ($a = 400$ nm, $d = 200$ nm) with the induced spectral weighting from Fig. 2 (b), named ‘Spectrum B’ here. This design serves as the reference for the variations. (a) Excitation spectrum $G(\lambda)$ conveyed by the time-domain excitation signal during optimization. The region of interest (ROI) 300–700 nm to evaluate broadband performance is marked in yellow. (b) Illustration of the optimized metasurfaces for each parametric variation, showing a section in the top-view. They all share the same length scale for comparability. (c) Comparison of the absorption spectra within the ROI for the optimized metasurfaces under each variation.

power dissipation. We explored the physical effects on broadband performance that inherently arise from a metasurface’s periodic array configuration. It was observed that dimensional parameters and spectral weighting can be tailored to enhance absorption in towards red, where the improvement is primarily dictated by lattice-induced effects. All designs evolved into all-connected metasurfaces, characterized by a complex interwoven network of waveguide-like structures. These topologies enabled high broadband absorption based on a complex interplay of physical phenomena. They motivate an in-depth analytical examination and can furthermore inspire conventional and other inverse design approaches. We therefore made these designs openly available.

We chose Silicon as a representative semiconducting material, as it is the most widely used in the semiconductor industry. However, our CCPR-ADE formulation also allows for optimization of other dispersive media. These include metals, making it suitable for designing thermoplasmonic metasurfaces - or combining both dielectric and plasmonic materials for hybrid configurations.

Employing the time-domain adjoint method for nanophotonic inverse design is rarely reported in the literature, in contrast to its widely used frequency-domain counterpart. Our results highlight

the power of the time-domain approach in achieving broadband performance, motivating further exploration and application to other photonic systems.

APPENDIX A

ON A QUANTITATIVE BROADBAND MEASURE

We introduce here a simple quantitative measure of broadband performance that takes into account the sharp features and rapid fluctuations in the absorption spectra in Fig. 5.

The simplest way to quantify enhanced absorption is to compute the average $\langle Q_{\text{abs}} \rangle$, evaluated over the wavelength range of interest. However, this metric alone does not capture spectral variations, making it unable to distinguish between a uniformly broadband response and a narrow peak. To address this limitation, we additionally evaluate the fractional bandwidth B_F and the root mean square deviation (RMSD) with respect to a smoothed signal. To suppress sharp oscillations in the absorption spectra, we apply a low-pass filter on the spectra. Specifically, we choose a 4th-order Butterworth filter with (normalized) cutoff frequency 0.05 [29] (using `Scipy’s butter`), as illustrated in Fig. 6. This filtering ensures a stable measure of B_F and quantification of variations in the

(original) absorption spectrum. The RMSD provides a statistical measure of fluctuations across the entire wavelength range, while the fractional bandwidth B_F characterizes the relative spectral range where absorption remains significant ($A > 0.5$). Together with the average, these three parameters establish a systematic quantitative evaluation of broadband performance.

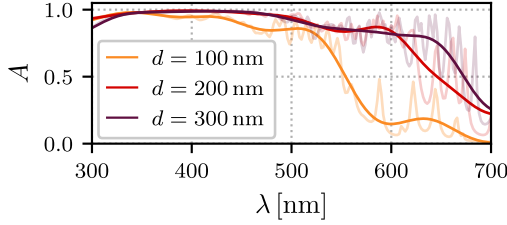


Fig. 6: Smoothed absorption spectra, using a Butterworth low-pass filter. Herein, applied to the spectra from Fig. 5 (mid row) for demonstration. Based on this filtering, we calculated the RMSD and B_F listed in Table II.

	Parameters (a , d , Exc.)	$\langle Q_{\text{abs}} \rangle$	B_F	RMSD
Reference	(400 nm, 200 nm, B)	0.824	0.732	0.085
Periodicity	(200 nm, 200 nm, B)	0.737	0.684	0.045
	(600 nm, 200 nm, B)	0.793	0.715	0.074
Thickness	(400 nm, 100 nm, B)	0.625	0.595	0.063
	(400 nm, 300 nm, B)	0.856	0.768	0.083
Excitation	(400 nm, 200 nm, A)	0.549	0.582	0.084
	(400 nm, 200 nm, C)	0.823	0.755	0.091

TABLE II: Average $\langle Q_{\text{abs}} \rangle$, fractional bandwidth B_F , and the root mean square deviation (RMSD) of the absorption spectra from Fig. 5. B_F and RMSD were computed with respect to a low-pass filtered signal (Fig. 6).

Table II summarizes these quantities for the absorption spectra presented in Fig. 5. From that, we can state that the design with $d = 300$ nm exhibits the overall best broadband performance, as indicated by the largest values of both $\langle Q_{\text{abs}} \rangle$ and B_F . In contrast, the structure evolved under the excitation spectrum ‘A’ performs the worst. A relatively high RMSD they both have in common is caused by the rapid variations in the red regime, which we attributed to lattice resonances.

REFERENCES

- [1] L. Mascaretti, Y. Chen, O. Henrotte, O. Yesilyurt, V. M. Shalaev, A. Naldoni, and A. Boltasseva, “Designing metasurfaces for efficient solar energy conversion,” *ACS Photonics*, vol. 10, no. 12, p. 4079–4103, Dec. 2023.
- [2] E. Cortés, F. Wendisch, L. Sortino, A. Mancini, S. Ezendam, S. Saris, L. Menezes, A. Tittl, H. Ren, and S. Maier, “Optical metasurfaces for energy conversion,” *Chemical Reviews*, vol. 122, 06 2022.
- [3] C.-C. Chang, W. J. M. Kort-Kamp, J. Nogan, T. S. Luk, A. K. Azad, A. J. Taylor, D. A. R. Dalvit, M. Sykora, and H.-T. Chen, “High-temperature refractory metasurfaces for solar thermophotovoltaic energy harvesting,” *Nano Letters*, vol. 18, no. 12, p. 7665–7673, Nov. 2018.
- [4] Z. Chen, Z. Wen, Z. Wu, Y. Gao, C. Tan, Z. Deng, X. Li, D. Zhou, F. Liu, J. Hao, Z. Huang, N. Dai, and Y. Sun, “Inverse-designed broadband ultrathin aperiodic metacoatings spanning from deep ultraviolet to near infrared,” *Laser & Photonics Reviews*, 2024.
- [5] P. Zhu and L. Jay Guo, “High performance broadband absorber in the visible band by engineered dispersion and geometry of a metal-dielectric-metal stack,” *Appl. Phys. Lett.*, vol. 101, no. 24, Dec. 2012.
- [6] A. Azad, W. Kort-Kamp, M. Sykora, N. Weisse-Bernstein, T. Luk, A. Taylor, D. Dalvit, and H.-T. Chen, “Metasurface broadband solar absorber,” *Sci. Rep.*, vol. 6, p. 20347, 2015.
- [7] R. A. Pala, S. Butun, K. Aydin, and H. A. Atwater, “Omnidirectional and broadband absorption enhancement from trapezoidal mie resonators in semiconductor metasurfaces,” *Sci. Rep.*, vol. 6, no. 1, Sep. 2016.
- [8] P. D. Terekhov, K. V. Baryshnikova, Y. Greenberg, Y. H. Fu, A. B. Evlyukhin, A. S. Shalin, and A. Karabchevsky, “Enhanced absorption in all-dielectric metasurfaces due to magnetic dipole excitation,” *Sci. Rep.*, vol. 9, no. 1, Mar. 2019.
- [9] J. Gedeon, I. Allayarov, A. Calà Lesina, and E. Hassan, “Time-domain topology optimization of power dissipation in dispersive dielectric and plasmonic nanostructures,” *IEEE Trans. Antennas Propag.*, pp. 1–1, 2025.
- [10] G. W. Castellanos, P. Bai, and J. Gómez Rivas, “Lattice resonances in dielectric metasurfaces,” *J. Appl. Phys.*, vol. 125, no. 21, Jun. 2019.
- [11] Z. Li, R. Pestourie, Z. Lin, S. G. Johnson, and F. Capasso, “Empowering metasurfaces with inverse design: Principles and applications,” *ACS Photonics*, vol. 9, no. 7, p. 2178–2192, Jun. 2022.
- [12] A. M. Hammond, A. Oskooi, M. Chen, Z. Lin, S. G. Johnson, and S. E. Ralph, “High-performance hybrid time/frequency-domain topology optimization for large-scale photonics inverse design,” *Opt. Express*, vol. 30, no. 3, pp. 4467–4491, Jan 2022.
- [13] J. Gedeon, E. Hassan, and A. Calà Lesina, “Time-domain topology optimization of arbitrary dispersive materials for broadband 3D nanophotonics inverse design,” *ACS Photonics*, vol. 10, no. 11, pp. 3875–3887, 2023.
- [14] K. P. Prokopidis and D. C. Zografopoulos, “Time-domain studies of general dispersive anisotropic media by the complex-conjugate pole-residue pairs model,” *Applied Sciences*, vol. 11, no. 9, 2021.
- [15] C. Schinke, C. Peest, J. Schmidt, R. Brendel, M. R. Vogt, I. Kröger, S. Winter, A. Schirmacher, S. Lim, H. Nguyen, and D. Macdonald, “Uncertainty analysis for the coefficient of band-to-band absorption of crystalline silicon,” *AIP Advances*, vol. 5, p. 067168, 06 2015.
- [16] M. Han, R. Dutton, and S. Fan, “Model dispersive media in finite-difference time-domain method with complex-conjugate pole-residue pairs,” *IEEE Microw. Wirel. Compon. Lett.*, vol. 16, no. 3, pp. 119–121, 2006.
- [17] M. P. Bendsøe and O. Sigmund, *Topology Optimization – Theory, Methods, and Applications*. Germany: Springer Verlag, 2003.
- [18] A. Taflove and S. C. Hagness, *Computational electrodynamics: the finite-difference time-domain method*, 3rd ed. Norwood: Artech House, 2005.
- [19] L. Landau, E. Lifshitz, and L. Pitaevskii, *Electrodynamics of Continuous Media: Volume 8*, ser. Course of theoretical physics. Elsevier Science, 1995.
- [20] Ansys Lumerical Inc., “FDTD: 3D Electromagnetic Simulator,” Software, 2024, available: <https://www.ansys.com/products/optics/fdtd>.
- [21] A. C. Lesina, A. Vaccari, P. Berini, and L. Ramunno, “On the convergence and accuracy of the FDTD method for nanoplasmonics,” *Opt. Express*, vol. 23, no. 8, pp. 10 481–10 497, Apr 2015.
- [22] J. Gedeon, “Topology optimized metasurfaces,” 2025, dataset. [Online]. Available: <https://doi.org/10.5281/zenodo.14903141>
- [23] F. Wang, B. S. Lazarov, and O. Sigmund, “On projection methods, convergence and robust formulations in topology optimization,” *Structural and Multidisciplinary Optimization*, vol. 43, pp. 767–784, 2011.
- [24] Z. Dong, T. Wang, X. Chi, J. Ho, C. Tserkezis, S. L. K. Yap, A. Rusydi, F. Tjijtoharsono, D. Thian, N. A. Mortensen, and J. K. W. Yang, “Ultraviolet interband plasmonics with Si nanostructures,” *Nano Lett.*, vol. 19, no. 11, p. 8040–8048, Sep. 2019.
- [25] A. Ndao, R. Salut, M. Suarez, and F. I. Baida, “Plasmonless polarization-selective metasurfaces in the visible range,” *Journal of Optics*, vol. 20, no. 4, p. 045003, mar 2018.
- [26] J. A. Garcia, C. Hrelescu, X. Zhang, D. Grosso, M. Abbarchi, and A. L. Bradley, “Quasi-guided modes in titanium dioxide arrays fabricated via soft nanoimprint lithography,” *ACS Appl. Mater. Interfaces*, vol. 13, no. 40, pp. 47 860–47 870, Sep. 2021.
- [27] O. D. Miller, A. G. Polimeridis, M. T. H. Reid, C. W. Hsu, B. G. DeLacy, J. D. Joannopoulos, M. Soljačić, and S. G. Johnson, “Fundamental limits to optical response in absorptive systems,” *Opt. Express*, vol. 24, no. 4, pp. 3329–3364, Feb 2016.
- [28] Z. Yu, A. Raman, and S. Fan, “Fundamental limit of nanophotonic light trapping in solar cells,” *Proceedings of the National Academy of Sciences*, vol. 107, no. 41, pp. 17 491–17 496, 2010.
- [29] S. Butterworth, “On the Theory of Filter Amplifiers,” *Experimental Wireless & the Wireless Engineer*, vol. 7, pp. 536–541, Oct. 1930.